1-1-2019

Electrochemical CO2 reduction over nitrogen-doped SnO2 crystal surfaces

Yuefeng Zhang
Hunan University

Jianjun Liu
Hunan University

Zengxi Wei
Hunan University

Quanhui Liu
Hunan University

Caiyun Wang
University of Wollongong, caiyun@uow.edu.au

See next page for additional authors

Electrochemical CO2 reduction over nitrogen-doped SnO2 crystal surfaces

Abstract

Crystal planes of a catalyst play crucial role in determining the electrocatalytic performance for CO2reduction. The catalyst SnO2can convert CO2molecules into valuable formic acid (HCOOH). Incorporating heteroatom N into SnO2further improves its catalytic activity. To understand the mechanism and realize a highly efficient CO2-to-HCOOH conversion, we used density functional theory (DFT) to calculate the free energy of CO2reduction reactions (CO2RR) on different crystal planes of N-doped SnO2(N-SnO2). The results indicate that N-SnO2lowered the activation energy of intermediates leading to a better catalytic performance than pure SnO2. We also discovered that the N-SnO2(211) plane possesses the most suitable free energy during the reduction process, exhibiting the best catalytic ability for the CO2-to-HCOOH conversion. The intermediate of CO2RR on N-SnO2is HCOO* or COOH* instead of OCHO*. These results may provide useful insights into the mechanism of CO2RR, and promote the development of heteroatom-doped catalyst for efficient CO2RR.

Disciplines

Engineering | Physical Sciences and Mathematics

Publication Details

Zhang, Y., Liu, J., Wei, Z., Liu, Q., Wang, C. & Ma, J. (2019). Electrochemical CO2 reduction over nitrogen-doped SnO2 crystal surfaces. Journal of Energy Chemistry, 33 22-30.

Authors

Yuefeng Zhang, Jianjun Liu, Zengxi Wei, Quanhui Liu, Caiyun Wang, and Jianmin Ma

Electrochemical CO_2 reduction over nitrogen-doped SnO_2 crystal surfaces

Yuefeng Zhang[a,1], Jianjun Liu [a,1], Zengxi Wei [a], Quanhui Liu [a], Caiyun Wang [b], Jianmin Ma [a,*]

[a]*School of Physics and Electronics, Hunan University, Changsha 410082, Hunan, China*

[b]*ARC Centre of Excellence for Electromaterials Science, Intelligent Polymer Research Institute, AIIM Facility, University of Wollongong, North Wollongong, NSW 2500, Australia*

[1]These authors contributed equally to this work.

Corresponding author.

E-mail address: nanoelechem@hnu.edu.cn (J. Ma)

Abstract Crystal planes of a catalyst play crucial role in determining the electrocatalytic performance for CO_2 reduction. The catalyst SnO_2 can convert CO_2 molecules into valuable formic acid (HCOOH). Incorporating heteroatom N into SnO_2 further improves its catalytic activity. To understand the mechanism and realize a highly efficient CO_2-to-HCOOH conversion, we used density functional theory (DFT) to calculate the free energy of CO_2 reduction reactions (CO_2RR) on different crystal planes of N-doped SnO_2 (N-SnO_2). The results indicate that N-SnO_2 lowered the activation energy of intermediates leading to a better catalytic performance than pure SnO_2. We also discovered that the N-SnO_2 (211) plane possesses the most suitable free energy during the reduction process, exhibiting the best catalytic ability for the CO_2-to-HCOOH conversion. The intermediate of CO_2RR on N-SnO_2 is HCOO* or COOH* instead of OCHO*. These results may provide useful insights into the mechanism of CO_2RR, and promote the development of heteroatom-doped catalyst for efficient CO_2RR.

Key words: CO_2 reduction reaction; SnO_2; Crystal surface; Electrocatalysis; First principles

1. Introduction

Electrochemical CO_2 reduction reaction has attracted great interest, since it can convert the greenhouse gas CO_2 into value-added products and liquid fuels [1]. The CO_2-to-HCOOH conversion is a promising one due to the versatile applications of HCOOH in various fields. For example, HCOOH as a chemical can be used in the industry of printing, dyeing, medicine and textile [2]. HCOOH is also a medium for producing hydrogen [3] as a potential source for fuel cell [4]. The reported catalysts for the CO_2-to-HCOOH conversion include Hg, In, Pd, Sn, Bi, Cd, Tl, Co_3O_4 and SnO_2 [5]. Among these catalysts, SnO_2 holds great promise because of its high selectivity, cost-effectiveness, environmental friendliness, and outstanding thermal stability [6]. For example, a hierarchical SnO_2 microsphere catalyst demonstrated a remarkable catalytic activity and selectivity due to its hierarchical structure with abundant active sites for boosting the CO_2RR [7]. A mesoporous SnO_2 electrocatalyst could convert CO_2 to HCOOH at low overpotentials, which can be ascribed to its high oxygen vacancy defects, facilitating the absorption of CO_2 [8]. Moreover, Li et al. proved that N-doped SnO_2 catalyst possessed high catalytic activity and selectivity in converting CO_2 into HCOOH, which is due to the significantly increased electron transfer rate after N doping [9].

Tuning a catalyst by means of structure, size, morphology, grain boundary, composition can greatly improve its electrocatalytic performance [10]. The structural characteristics of specific facet can enhance the catalytic efficiency as well. For example, Won et al. reported that the (101) facet of Zn electrode showed more potentials for reducing CO_2 to CO than its (002) facet [11]. This is due to that the (110) facet of Zn not only has the lower reduction potential for CO_2 reduction to CO, but also has higher energy barrier for HER than (002) face. Rosen et al. found that the (211) and (110) facets of Ag were favorable to CO_2 reduction than its (100) and (111) facets, because the (211) and (110) facets of Ag show distinctly lower free energy for the rate-limiting step in CO_2 RR than the (100) and (111) facets [12]. However, the mechanism of CO_2 RR on the different surfaces of SnO_2 is not reported yet. Therefore, it is imperative to study the nature of CO_2 RR on different crystal planes of SnO_2.

In this work, we chose the following three crystal planes of SnO_2 as the subjects: (1 1 0), (1 0 1), and (2 1 1). They were cleaved from the optimized SnO_2 bulk. These three planes encompass higher peaks in the XRD pattern than others [13], which indicate that these crystal facets are relatively stable and easy to be exposed during the synthesis process. Furthermore, we chose oxygen atoms, which could be replaced by the N atom, as the terminated surfaces for different crystal faces. We studied the mechanism of CO_2 RR over the N-doped (1 1 0), (1 0 1) and (2 1 1) planes of SnO_2 with the aid of DFT calculations. By means of estimating the reaction energies for various intermediates on these different SnO_2 crystal planes, we have obtained some interesting information about the stability of these adsorbents in the reaction process as well as the catalytic nature for nitrogen doping on different SnO_2 crystal planes.

2 Experimental

2.1 Calculation methods

The structure optimizations and energy calculations were performed using Vienna *ab initio* simulation package (VASP) [14, 15]. The exchange-correlation functional was described by the Perdew-Burke-Ernzerhof generalized gradient approximation (PBE-GGA) method [16], and interaction between core electrons and valence electrons was described using the frozen-core projector-augmented wave (PAW) method. Wave functions were expanded in a plane wave basis with a high energy cut-off of 450 eV, and k-space was sampled by a grid of 3 × 3 × 1; at the same time, we set the value of sigma to 0.02 eV. The convergence criterion was set to 10^{-5} eV between two ionic steps for the self-consistency process, and 0.02 eV/Å was adopted for the total energy calculations. Additionally, we have set a vacuum region of 15 Å along the normal direction to avoid interactions between adjacent images.

2.2 Model

In this study, rutile SnO_2 with an optimized lattice constant (a = 4.737 Å, b = 4.737 Å, and c = 3.186 Å) was chosen for the electrocatalytic CO_2 RR. The specific structure is shown in Fig. 1(a and b). Fig. 1(c) shows the band structure of SnO_2 along the high symmetry axis of crystal Brillouin zone [17]. We can easily find that SnO_2 was a semiconductor with a direct band gap of 3.606 eV,

because these two values emerged at the G point at the same time, which is consistent with the values obtained in the experiment [18]. The density of state (DOS) of SnO_2 is displayed in Fig. 1(d). Similarly, when the Fermi level was set to 0 eV, the band gap was 3.606 eV, which is well agreed with the value measured by the band structure. Due to the fact that the electrons near Fermi energy have a major influence on the material, the deep-level electronic status is not taken into consideration. In this picture, we can see the following part of the Fermi level, namely the valence band, which was mainly the contribution of O with minor portion from Sn. However, in the conduction band area, the situation was exactly the opposite: Sn contributed more than O.

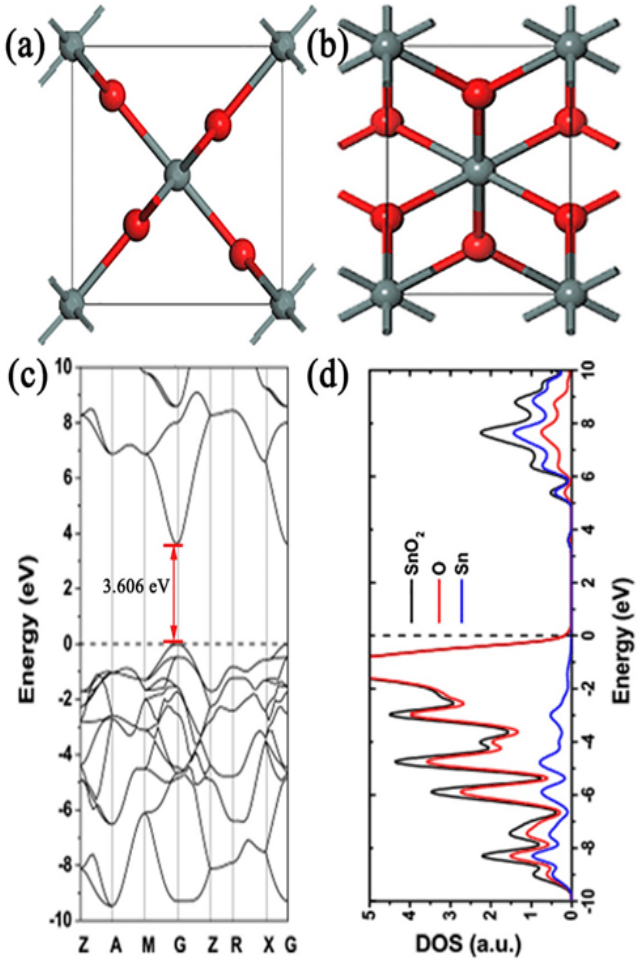

Fig. 1. (a) Top view and (b) side view of SnO_2 bulk structure. The related electronic properties of SnO_2: (c) band structure and (d) density of state. The black, red and blue lines correspond to the total DOS as well as the O and Sn of PDOS for SnO_2, respectively. The Fermi level was set to be 0

eV. The greyish-green and red balls represent Sn and O atoms, respectively.

2.3. Reaction path and free energy

It is a two-electron reaction involved in the CO_2-to-HCOOH conversion process, which indicates that this process requires less energy input than the multi-electron reduction processes for CH_4, C_2H_4 or more complex hydrocarbons. The following formula is the CO_2RR path on different crystal facets of SnO_2:

$$CO_2(g) + 2(H^+ + e^-) + * \rightarrow HCOO^*/OCHO^*/\ COOH^* + (H^+ + e^-) \rightarrow * + HCOOH(l)$$

Where "*" denotes an adsorption site on the surface. CO_2 is in the gas phase, HCOO* /OCHO*/COOH* stands for HCOO /OCHO/COOH in the adsorbed state, and HCOOH (l) represents formic acid formed.

We provided a method to calculate the free energy of different adsorbed substances in the process of electrocatalytic CO_2 RR. This method was based on the computational hydrogen electrode (CHE) model, which was first put forward by Nøskov et al. The CHE model involves the basic reaction mechanism on the Pt (111) facet. It not only explained why Pt is a commonly used electrode material, but also provided an approach to enhance the electrocatalytic performance of a fuel cell cathode [19]. The formula for calculating the Gibbs free energy for adsorbed species is as follows.

$$G = E + E_{\mathrm{ZPE}} - TS + G_{\mathrm{pH}}$$

Where E is the total energy of adsorbed species that can get from DFT. T corresponds to the constant temperature of the system with a value of 298.15 K. Consequently, we can calculate the changes in Gibbs free energy (ΔG) for all the adsorbed species on SnO_2 surface in different circumstances, according to the following formula：

$$\Delta G = \Delta E + \Delta E_{\mathrm{ZPE}} - T\Delta S + \Delta G_{\mathrm{pH}}$$

Here, ΔE corresponds to the binding energy of adsorbed species [20].

More specifically, the adsorption energy marked as E_{ad}, which are able to calculate the stability of the adsorption configurations [21]. Adsorption energy formula can be defined as follows:

$$E_{ad} = E_{adsorbate/surface} - E_{adsorbate} - E_{surface}$$

Here, $E_{adsorbate/surface}$, $E_{adsorbate}$ and $E_{surface}$ represent total energy of the system of adsorbate and surface, adsorbate in vacuum, bare surface, respectively. If E_{ad} is negative, it indicates that the adsorption process is exothermic [22]. ΔE_{ZPE} is the difference in the zero point energy and ΔS is the change in entropy. Calculating the zero point energy is the summation of the vibration frequencies of all atoms for any system, and the corresponding formula is: $E_{ZPE} = 1/2\Sigma\hbar\nu$. The entropy for free molecules is derived from the NIST database. However, this part of the value can be ignored by fixing the SnO_2 crystal plane under different situations. Due to $\Delta G_{pH} = 2.303 k_B T \mathrm{pH}$, in this work, we suppose that pH = 0, hence $\Delta G_{pH} = 0$ [23].

3. Results and discussion

3.1 Band structure

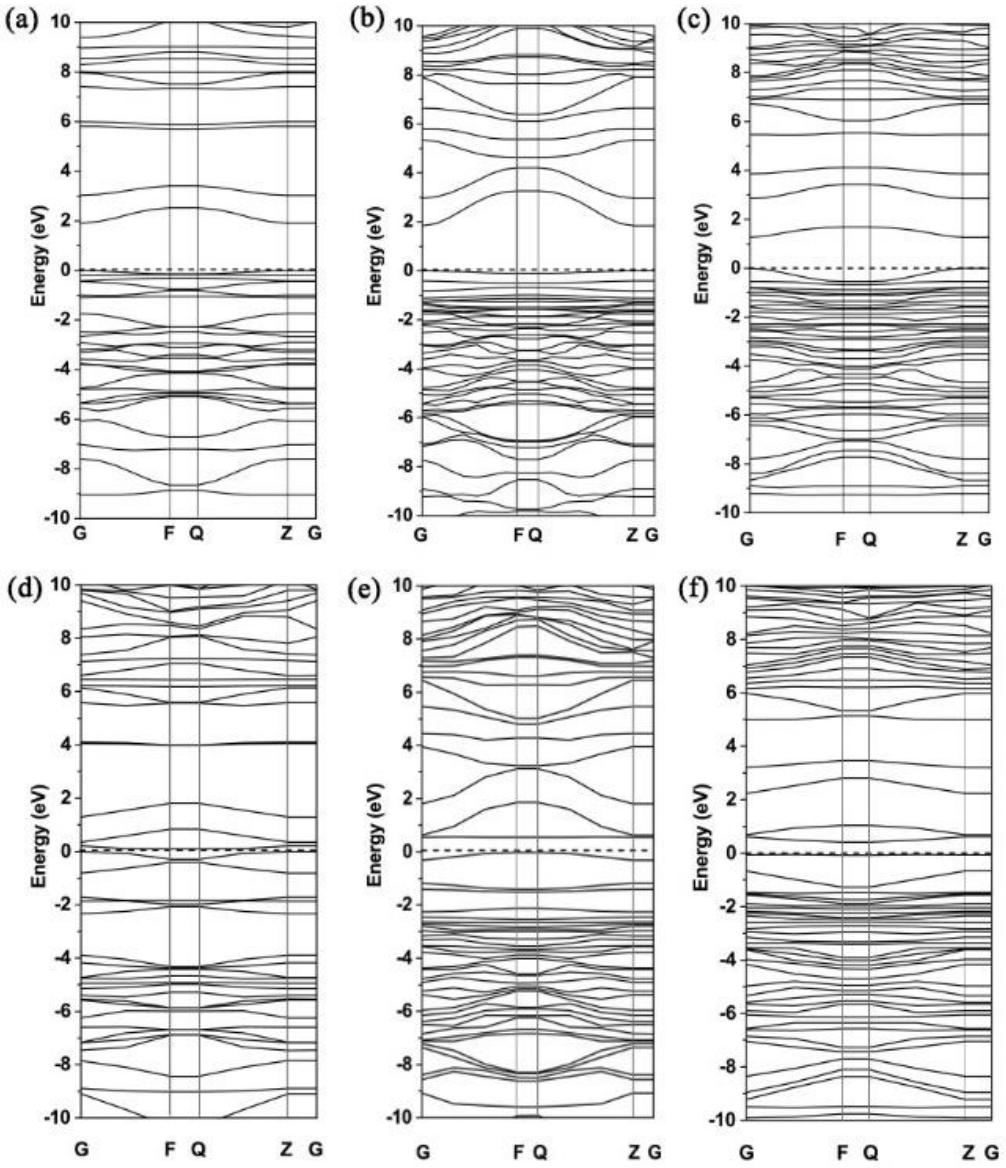

Fig. 2. The band structure diagram of different crystal surfaces of SnO_2: (a) SnO_2 (110), (b) SnO_2 (101), (c) SnO_2 (211), (d) N-SnO_2 (110), (e) N-SnO_2 (101) and (f) N-SnO_2 (211). The dotted line is match along with the Fermi level.

The band structure of different surfaces of SnO_2 (110) is reflected in Fig. 2(a). It can be seen that it was a direct band gap semiconductor material with E_g=1.903 eV at G, which is the geometric points in the reciprocal space. And its valence band was almost provided by O 2*p* orbital. The band structure of SnO_2 (101) can be observed in Fig. 2(b). Similar to the (110) plane, SnO_2 (101) facets also possessed a direct band gap with E_g= 1.836 eV at G. Fig. 2(c) shows the band structure of the

SnO_2 (211) facet. Similarly, the bottom of CB and top of VB were situated at the G point with E_g=1.266 eV. In Fig. 2(d), the position of the minimum value of the conduction band and the maximum value of the valence band was not at the same high symmetry point, so it was an indirect band gap (E_g=0.096 eV). It means that electrons jump from the valence band to the conduction band not only absorb energy, but also change the momentum. Comparing Fig. 2(a and d), we can find that the N-doping induced a significant decrease in the band gap value. The emergence of this phenomenon is due to the fact that N doped atoms lead to shifts in the conduction band and valence band. The band structure of N-SnO_2 (101) plane was presented in Fig. 2(e), which is illustrated as that the summit of the valance band and the lowest of conduction band fell at the Q point simultaneously. Therefore, it was a direct gap semiconductor with a band gap of 0.467 eV. The band structure of N-SnO_2 (211) surface is expressed in Fig. 2(f), and it is a direct band gap. Its E_g was 0.295 eV, smaller than that of SnO_2 (211). The reduction of the bandgap value essentially improves the conductivity of the material and facilitates the CO_2 RR. All these results clearly demonstrate that the band gap values of different crystal surfaces were decreased because of the production of the defective energy level after the N-doping. It also indicates that the N-doped SnO_2 may afford improved catalytic activity to the CO_2-HCOOH conversion compared with pure SnO_2.

3.2 Density of states

To further understand the changes in the catalytic properties caused by N-doping on different crystal faces of SnO_2, the density of state (DOS) was calculated and shown in Fig. 3. Fig. 3(a, c and e) shows the total DOS and the projected density of states (PDOS) of SnO_2 (110), SnO_2 (101), SnO_2 (211), respectively. By analyzing these three diagrams, we can find that the energy level in valence band mainly originated from O 2*p* orbits, and the contribution of Sn 5*d* orbits in the valence band portion was very small. Nevertheless, Sn 5*d* orbits played a key role in the conduction band compared to O 2*p* orbits. The total DOS and PDOS of N-SnO_2 (110) are analyzed in Fig. 3(b). It is apparent that the energy levels closing to the Fermi level were mainly provided by N atom. Moreover, the band gap value after nitrogen doping is reduced much compared to the undoped case, indicating a considerable enhancement in the conductivity of N-doping. Fig. 3(d) delivers the DOS of N-SnO_2 (101). Clearly, the conduction band moved toward low energy with respect to SnO_2 (101),

so the band gap value became very small. The DOS of N-SnO_2 (211) facet is displayed in Fig. 3(f). Notably, when accessing to the Fermi energy level, the conduction band mainly consisted of N atoms. Because the hybridization occurred among the orbits of O, Sn, and N, hence, a new electronic occupation emerged around Fermi level, which makes electronic transitions easier. Overall, through the above analysis of DOS data, we can draw a conclusion that the incorporation of N atoms can lessen the band gap value, which is beneficial for charge transfer. Thus, it makes electrocatalytic CO_2 RR more efficient.

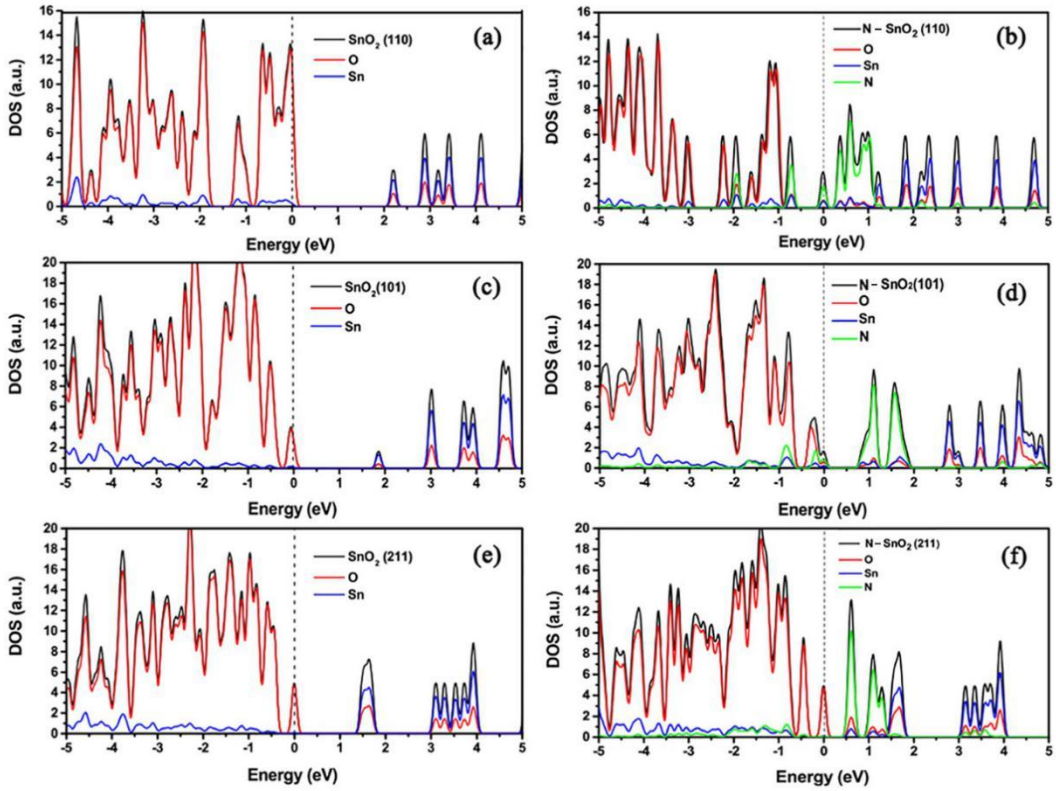

Fig. 3. Density of state for different facets of the SnO_2: (a) SnO_2 (110), (b) N-SnO_2 (110), (c) SnO_2 (101), (d) N-SnO_2 (101), (e) SnO_2 (211) and (f) N-SnO_2 (211). Fermi level is represented by a dotted line.

3.3 CO_2 reduction reaction

The calculated free energy diagrams of CO_2 RR on these various SnO_2 facets including undoped and N-doped states are displayed in Fig. 4(a-f). In terms of a kinetic model, the ideal H atom reaction energy value should be close to zero for HER [19]. Thus, taking it into consideration, we believe

that the closer the free energy is to zero, the better the catalytic effect. CO_2 was firstly hydrogenated through proton-coupled electron transfer in the process of the CO_2 RR [24]. We can find that the intermediate product OCHO* was formed and both O atoms were bound to the Sn atoms at the SnO_2 surface (Fig. 4a, c and e). After the doping of N, the N atom became the active sites for adsorbate. The intermediate product HCOO* or COOH* was formed on the N-SnO_2 plane (Fig. 4b, d and f). The change in this site is due to the fact that N atom formed covalent bonds with Sn atom after it replaced O atom. However, since the number of nuclear charges of O is one more than that of N. Thus, it formed a hole naturally and can accept a valence electron so that N site have higher chemical activity. Additionally, we have found that the N-doping could reduce the adsorption energy of HCOO*, which is in favor of the release of HCOOH. From the free energy profile, each individual process is an exothermic reaction, indicating that it can be spontaneously performed in addition to the N-SnO_2 (101) facet (Fig. 4d). Among them, the SnO_2 (101) plane released more heat (4.49 eV, Fig. 4c), suggesting that CO_2 was easy to get hydrogenated and then bound with this surface. In the other hand, this value was too large and the interaction force was so strong that the intermediates could not be easily desorbed from the surface to form HCOOH.

Once HCOO*(OCHO*) is formed, it will further couple the second H^+/e^-, generating either an adsorbed HCOOH* species or HCOOH(aq). In this hydrogenation step, it is exothermic with respect to the N-doped facets and endothermic for the undoped case. In the endothermic reaction, the intermediate OCHO* on the SnO_2 (110) (Fig. 4a) requires to absorb the most energy to be desorbed forming HCOOH. There is no doubt that it was the rate-limiting step in the entire reaction of the SnO_2 (110) planes. Similarly, for SnO_2 (101) (Fig. 4c) and SnO_2 (211) (Fig. 4e), the rate-limiting step was also the second proton coupled electron process. Thus we can draw a conclusion that the free energy of the reactions was changed after the introduction of N atoms. In contrast to the reaction from OCHO* to HCOOH on SnO_2, the N-SnO_2 underwent an exothermic process from HCOO*(COOH*) to HCOOH. However, in Fig. 4(d), the rate-limiting step corresponds to the process of first coupling proton and electrons. It is due to the fact that the step was uphill, which indicates that the protonation process was an endothermic reaction. Although the reaction energy is a positive value, it was very small so that it is achievable for proceeding the next catalytic reaction.

In short, the dopant of N induced the HCOO*(COOH*) production (an oxygen atom combined with a nitrogen atom), which reduced the interaction between the intermediate product and the interface. Thereby it facilitated the spontaneous reaction of the next step. In these N-doped surfaces, N-SnO_2(211) is in possession of the best catalytic effect. This is because not only its reaction energy value was close to zero, but also the reaction was exothermic (spontaneous reaction) for every step.

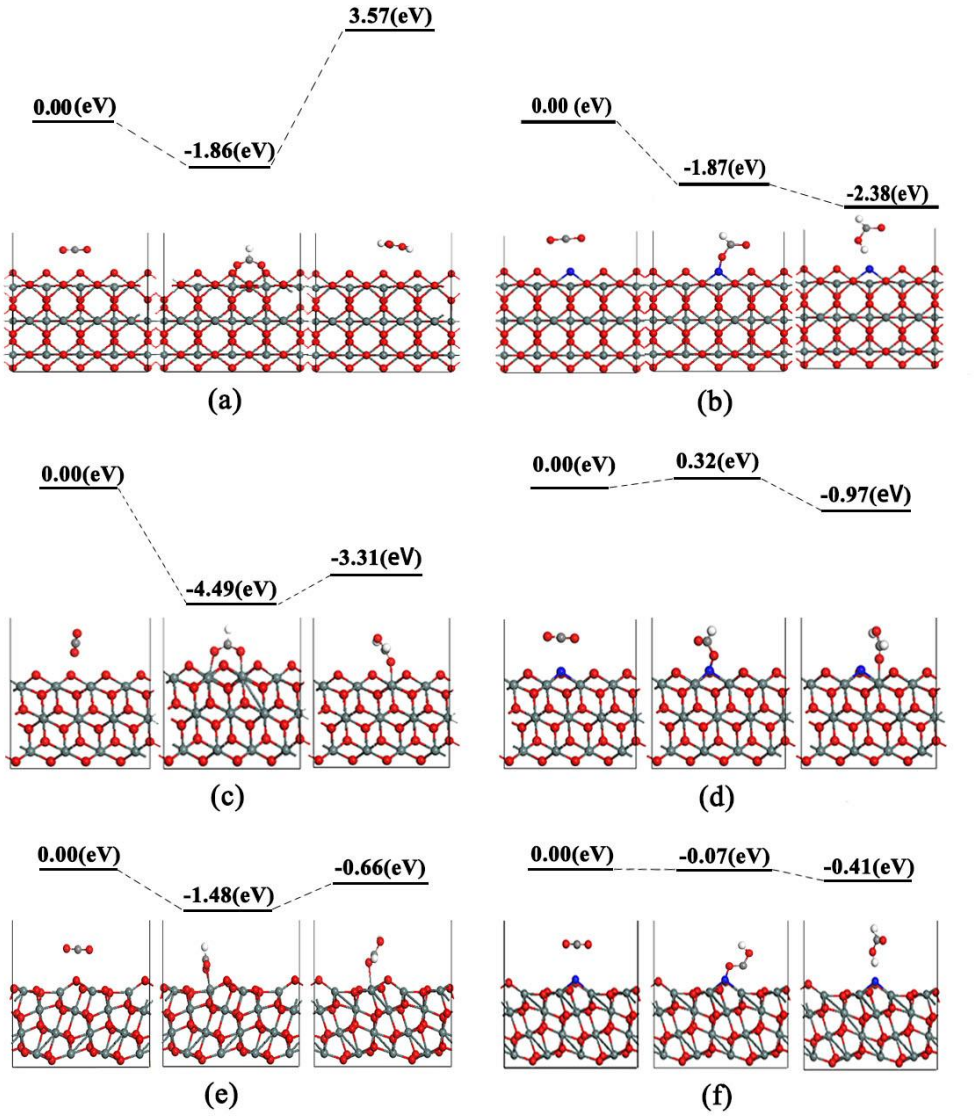

Fig. 4. The free energy of the CO_2 RR on different crystal facets: (a) SnO_2 (110), (b) N-SnO_2 (110), (c) SnO_2 (101), (d) N-SnO_2 (101), (e) SnO_2 (211) and (f) N-SnO_2 (211). This picture displays the

optimized crystal structure. The red, gray, white, blue, greyish-green balls represent O, C, H, N, Sn atom, respectively.

3.4 The projected density of the states

In order to understand the catalytic activity of SnO_2 and N-doped SnO_2 for the CO_2 RR, the projected density of states (PDOS) of the intermediate on various crystal facets of SnO_2 and N-doped SnO_2 was analyzed in Fig. 5. Comparing the three graphs of undoped situation (Fig. 5a, c, e), we can find that the span of state density peak is quite large. This means that the intermediate OCHO* and Sn atom have stronger delocalization and stronger bonds, and thus it is hard to form HCOOH. Similarly, the hybridization between the HCOO* and N atom is stronger (Fig. 5b), indicating that their interaction is stronger, which is very much in line with the reaction energy value (as shown in Fig. 4). Interestingly, the coupling is weak between HCOO* or COOH* and N atom (Fig. 5d, f); therefore, it is easy to generate HCOOH showing good catalytic performance.

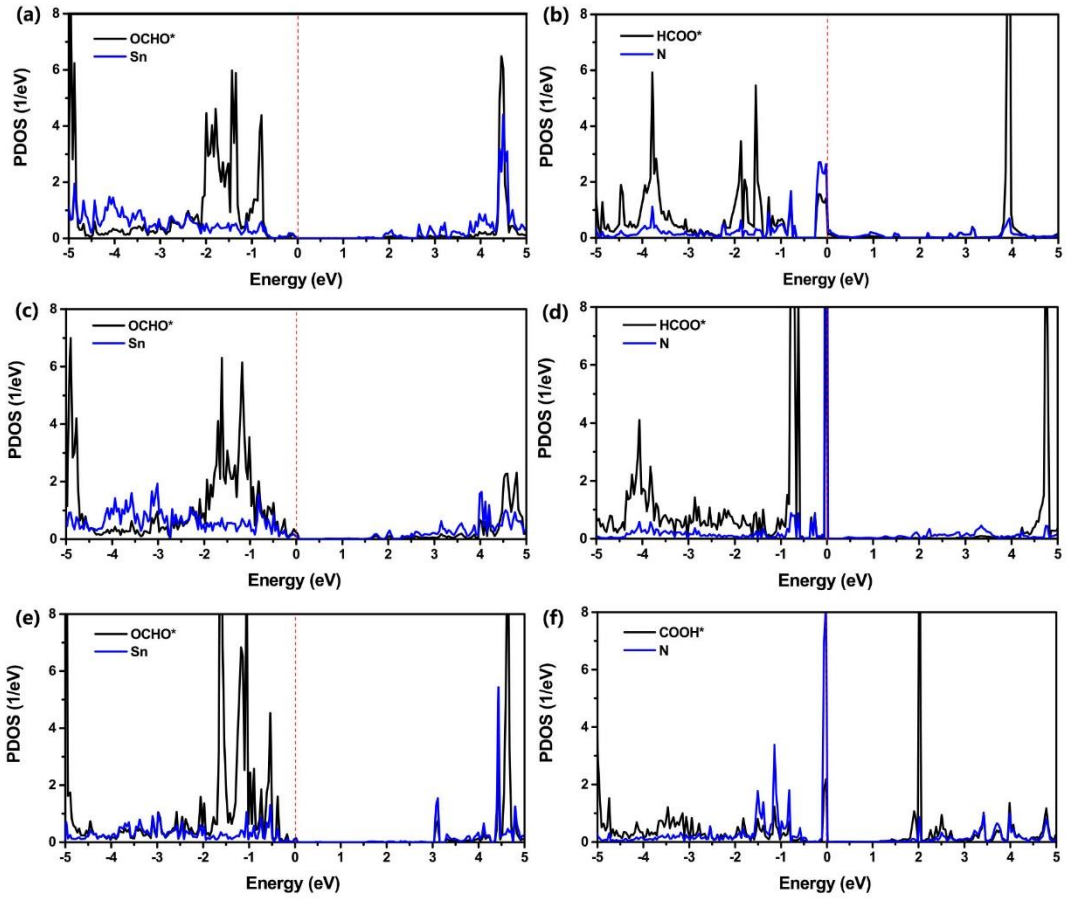

Fig. 5. The projected density of states of intermediate on various crystal surface of SnO_2: (a) SnO_2 (110), (b) N-SnO_2 (110), (c) SnO_2 (101), (d) N-SnO_2 (101), (e) SnO_2 (211) and (f) N-SnO_2 (211). The red dashed line corresponds to the Fermi level.

3.5 Charge density difference

For the purpose of acquiring a deeper understanding of electrons loss and gain, as well as the strength of the interaction between interface and species, we also visualized three dimensional charge density difference (Fig. 6) by the following formula [25]:

$$\Delta\rho = \rho_{\text{adsorbate/surface}} - \rho_{\text{adsorbate}} - \rho_{\text{surface}}$$

Here, $\rho_{\text{adsorbate/surface}}$, $\rho_{\text{adsorbate}}$ and ρ_{surface} correspond to the charge densities of the system of adsorbate at the surface, adsorbate in vacuum, and bare surface, respectively. Clearly, in Fig. 6(a1-f3), no any electron cloud was distributed at the bottom of the SnO_2 structure. This may be due to the large distance between the adsorption material and SnO_2 bottom resulting in low possibility of bonding. The electronic cloud was redistributed after the N doping. Fig. 6(a1-a3) displays that C atom was easy to donate electrons and O atom was easy to accept electrons due to the stronger electron affinity of O atom compared to C atom. Additionally, we find that after OCHO adsorbed on the surface SnO_2 (110), the distribution of electronic clouds was larger than others. It coincides with the Bader charge. Fig. 6(b1-b3) demonstrates the charge density difference of CO_2, HCOO and HCOOH adsorbed on the plane of N-SnO_2 (110), respectively. After the N doping, the valence electrons taken away by O atoms were more than the valence electrons introduced by N atoms due to higher electronegativity of O atom. Thus the SnO_2 (110) turned into a p-type species with electron-deficient. The charge density difference of SnO_2 (101) (Fig. 6c1-c3) was used in conjunction with N-SnO_2 (101) (Fig. 6d1-d3). We can catch sight of a phenomenon that the N-doping induced larger electron cloud between the interface of SnO_2 and the adsorbed material, suggesting that the gain and loss of electrons became bigger and bonded strongly; that is to say, the catalytic efficiency was straightened. Fig. 6(e1-e3) demonstrates that O atoms were prone to obtain electron from C atom. The distribution of electron clouds directly implies that the electron transfer was from Sn to O atoms. Fig. 6(f1-f3) reflectes the charge density difference of CO_2, COOH,

HCOOH adsorbed on the plane of N-SnO_2 (211), respectively. Interestingly, in spite of the fact that the N-SnO_2 (211) face generated COOH instead of HCOO, the final product remained unchanged, i.e., HCOOH. The fact is that COOH is commonly regarded as an intermediate for CO generation.

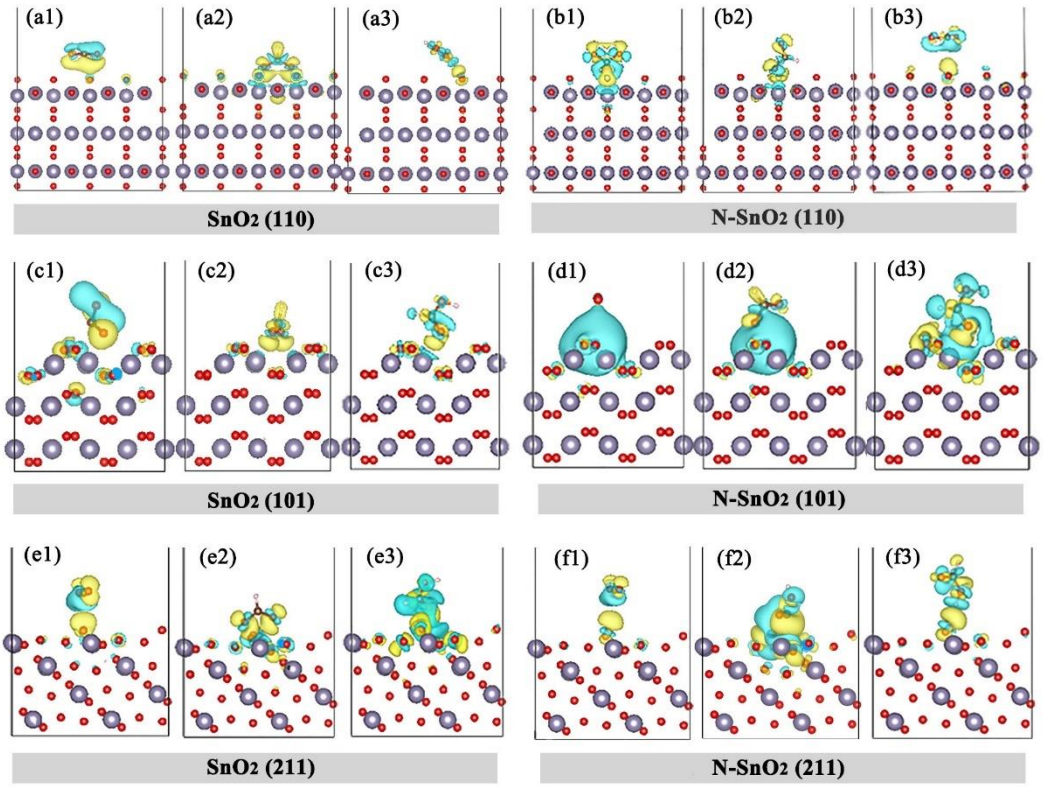

Fig. 6. The charge density difference of the reduction process of SnO_2 and N-doped SnO_2: (a1-a3) SnO_2 (110); (b1-b3) SnO_2 (101); (c1-c3) SnO_2 (211); (d1-d3) N-SnO_2 (110); (e1-e3) N-SnO_2 (101); and (f1-f3) N-SnO_2 (211). Yellow and blue electron clouds indicate charge accumulation and charge depletion, respectively. The isosurface value is set to 0.001 $eÅ^{-3}$.

3.6 Bader charge

In order to further understand the changes in the amount of interfacial charge transfer during CO_2, HCOO/OCHO/COOH, and HCOOH adsorption, we analyzed the Bader charge (Fig. 7a-f). Firstly, we can conclude from the whole graph that the gains and losses of electrons were conserved at each step of the entire reduction process. For example, when CO_2/HCOO adsorbed on the SnO_2(110) plane, it lost 0.163 eV and 0.533 eV, respectively. With HCOOH adsorbed on the SnO_2

plane, a 0.104 electron transferred from HCOOH to SnO_2 plane. We also found that each step of CO_2 RR had electron transfer, indicative of activated molecules. By analyzing the whole diagrams, it is evident that HCOO/OCHO/COOH absorbed on the SnO_2 plane, and the change in charge gain and loss was relatively large compared with other two adsorbed substances (i.e., CO_2 and HCOOH). It also means that the interaction between the intermediate product and plane is strong.

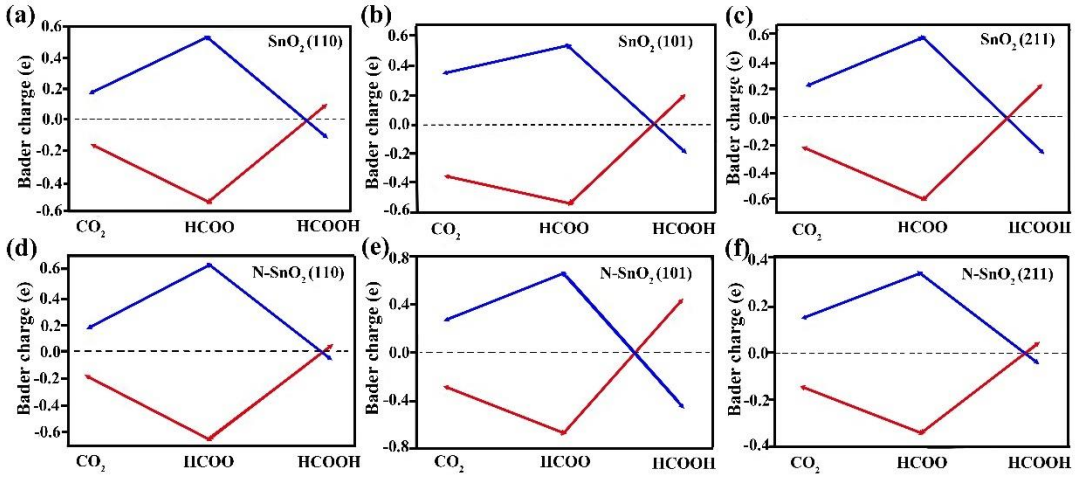

Fig. 7. (a) SnO_2 (110), (b) SnO_2 (101), (c) SnO_2 (211), (d) N-SnO_2 (110), (e) N-SnO_2 (101) and (f) N-SnO_2 (211). In these figures, the three dots on the red line represent the change of charge of CO_2, HCOO, HCOOH, and the blue line corresponds to the change in charge of the entire crystal surface. Positive value is electronic loss, and negative value is electronic gains.

4. Conclusions

In conclusion, the mechanism for CO_2 RR on the crystal planes of N-SnO_2 has been studied by employing DFT method. We calculated the free energy of CO_2 RR on different crystal faces of N-SnO_2. The results indicate that N-SnO_2 (211) plane exhibits the best catalytic performance for the CO_2–HCOOH conversion. It can be attributed to the small reaction energy value that is closer to zero; moreover, this reaction can proceed spontaneously. The outcome from this work may offer a deeper level of understanding and provide some guidance for developing highly efficient catalysts for CO_2 RR.

Acknowledgments

This work was supported by the National Natural Science Foundation of China (51302079), and the Natural Science Foundation of Hunan Province (Grant No. 2017JJ1008).

References

1. X. Duan, J. Xu, Z. Wei, J. Ma, S. Guo, S. Wang, H. Liu, S. Dou, Adv. Mater. 29 (2017) 1701784.
2. D. Gao, H. Zhou, F. Cai, J. Wang, G. Wang, X. Bao, ACS Catal. 8 (2018) 1510-1519.
3. Y. X. Duan, F. L. Meng, K. H. Liu, S. S. Yi, S. J. Li, J. M. Yan, Q. Jiang, Adv. Mater. 30 (2018) 1706194.
4. B. Zhang, J. Zhang, J. Energy Chem. 26 (2017) 1050-1066.
5. C. Genovese, C. Ampelli, S. Perathoner, G. Centi, J. Energy Chem. 22 (2013) 202-213.
6. J. Yu, H. Liu, S. Song, Y. Wang, P. Tsiakaras, Appl. Catal. A: General 545 (2017) 159-166.
7. M. Grasemann, G. Laurenczy, Energy Environ. Sci. 5 (2012) 8171-8181.
8. N. M. Aslam, M. S. Masdar, S. K. Kamarudin, W. R. W. Daud, APCBEE Procedia 3 (2012) 33-39.
9. X. Yu, P. G. Pickup, J. Power Sources 182 (2008) 124-132.
10. G. A. El-Nagar, K. M. Dawood, M. S. El-Deab, B. E. Al-Andouli, Appl. Catal. B: Environmental 213 (2017) 118-126.
11. R. Zhang, W. Lv, L. Lei, Appl. Surf. Sci. 356 (2015) 24-29.
12. T. Shinagawa, G. O. Larrazábal, A. J. Martín, F. Krumeich, J. Pérezramírez, ACS Catal. 8 (2017) 837-844.
13. J. Wu, Y. Huang, W. Ye, Y. Li, Adv. Sci. 4 (2017) 1700194.
14. N. Han, Y. Wang, H. Yang, J. Deng, J. Wu, Y. Li, Y. Li, Nature Commun. 9 (2018) 1320.
15. K. H. Liu, H. X. Zhong, S. J. Li, Y. X. Duan, M. M. Shi, X. B. Zhang, J. M. Yan, Q. Jiang, Progress in Mater. Sci. 92 (2017) 64-111.
16. J. Zhang, F. Li, M. Xue, J. Li, X. Ma, L. Chen, X. Zhang, D. Macfarlane, Angew. Chem. 129 (2017) 14718.
17. S. Bashir, S. S. Hossain, S. U. Rahman, S. Ahmed, A. Al-Ahmed, M. M. Hossain, J. CO_2 Utilization 16 (2016) 346-353.
18. M. Manikandan, T. Tanabe, G. V. Ramesh, R. Kodiyath, S. Ueda, Y. Sakuma, Y. Homma, A. Dakshanamoorthy, K. Ariga, H. Abe, Phys. Chem. Chem. Phys. 18 (2016) 5932-5937.
19. G. Xu, L. Zhang, C. He, D. Ma, Z. Lu, Sens. Actuators B Chemical 221 (2015) 717-722.
20. Q. Li, J. Fu, W. Zhu, Z. Chen, B. Shen, L. Wu, Z. Xi, T. Wang, G. Lu, J. J. Zhu, J. Am. Chem. Soc. 139 (2017) 4290.
21. Y. Fu, Y. Li, X. Zhang, Y. Liu, J. Qiao, J. Zhang, D. P. Wilkinson, Appl. Energy 175 (2016) 536-544.
22. R. Daiyan, X. Lu, W. H. Saputera, H. N. Yun, R. Amal, ACS Sustain. Chem. Eng. 7 (2017) 2542-2550.
23. Q. Li, W. Zhuo, Z. Miao, P. Hou, K. Peng, J. Energy Chem. 26 (2017) 825-829.
24. R. Daiyan, X. Lu, H. N. Yun, R. Amal, Catal. Sci. Technol. 7 (2017) 2542-2550.
25. Q. Li, J. Fu, W. Zhu, Z. Chen, B. Shen, L. Wu, Z. Xi, T. Wang, G. Lu, J. J. Zhu, J. Am. Chem. Soc. 139 (2017) 4290-4293.

26. C. Dong, J. Fu, H. Liu, T. Ling, J. Yang, S. Z. Qiao, X. W. Du, J. Mater. Chem. A 5 (2017) 7184-7190.
27. D. H. Won, H. Shin, J. Koh, J. Chung, H. S. Lee, H. Kim, S. I. Woo, Angew. Chem. Int. Ed. 55 (2016) 9297-9300.
28. J. Rosen, G. S. Hutchings, Q. Lu, S. Rivera, Y. Zhou, D. G. Vlachos, F. Jiao, ACS Catal. 5 (2015) 150605133022004.
29. Z. Yang, H. Wang, W. Song, W. Wei, Q. Mu, B. Kong, P. Li, H. Yin, J. Colloid Interf. Sci. 486 (2016) 232-240.
30. Y. Fu, Y. Li, X. Zhang, Y. Liu, X. Zhou, J. Qiao, Chinese J. Catal 37 (2016) 1081-1088.
31. A. Rabis, D. Kramer, E. Fabbri, M. Worsdale, R. Kötz, T. J. Schmidt, J. Phys. Chem. C 118 (2014) 11292–11302.
32. M. Manikandan, T. Tanabe, G. V. Ramesh, R. Kodiyath, S. Ueda, Y. Sakuma, Y. Homma, A. Dakshanamoorthy, K. Ariga, H. Abe, Phys. Chem. Chem. Phys 18 (2016) 5932-5937.
33. Q. Fu, L. C. C. Rausseo, U. Martinez, P. I. Dahl, J. M. G. Lastra, P. E. Vullum, I. H. Svenum, T. Vegge, ACS Appl. Mater. Interf. 7 (2015) 27782-27795.
34. G. Kresse, J. Furthmüller, Phys Rev B Condens Matter 54 (1996) 11169-11186.
35. J. P. Perdew, K. Burke, M. Ernzerhof, Physical Review Letters 77 (1996) 3865-3868.
36. P. D. Borges, L. M. R. Scolfaro, H. W. L. Alves, E. F. D. S. Jr, Theor. Chem. Acc. 126 (2009) 39-44.
37. V. E. Henrich, P. A. Cox, U. Diebold, The Surface Science of Metal Oxides, Cambridge University Press, 48 (1994), 138-138.
38. J. K. Nørskov, J. Rossmeisl, A. Logadottir, L. Lindqvist, J. R. Kitchin, T. Bligaard, H. Jónsson, J. Phys. Chem. B 108 (2004) 17886-17892.
39. W. Sheng, S. Kattel, S. Yao, B. Yan, Z. Liang, C. Hawxhurst, Q. Wu, J. G. Chen, Energy Environ. Sci. 10 (2017) 1180-1185.
40. Z. Lu, D. Ma, L. Yang, X. Wang, G. Xu, Z. Yang, Phys. Chem. Chem. Phys 16 (2014) 12488-12494.
41. M. Guo, H. Yang, X. Jian, J. Li, Z. Liang, P. Han, Appl. Surf. Sci. 428 (2018) 851-860.
42. K. Wang, Z. Ye, C. Liu, D. Xi, C. Zhou, Z. Shi, H. Xia, G. Liu, G. Qiao, ACS Appl. Mater. Interfaces 8 (2016) 2910-2916.
43. A. J. Göttle, M. T. M. Koper, Chem. Sci. 8 (2017) 458-465.
44. Z. Wei, Y. Zhang, S. Wang, C. Wang, J. Ma, J. Mater. Chem A 6 (2018) 13790-13796.

TOC

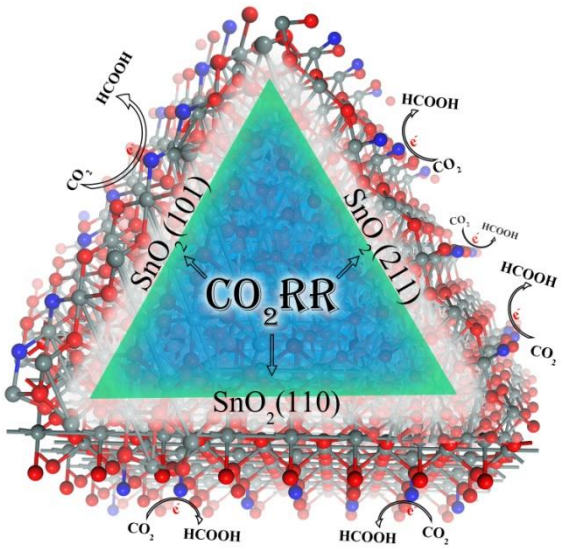

In this work, we have studied the mechanism of CO_2 RR over the N-doped (110), (101) and (211) surfaces of SnO_2. we used density functional theory (DFT) to calculate the free energy of each CO_2 reduction reaction (CO_2 RR) over (110), (101) and (211) crystal surfaces of N-doped SnO_2 (N-SnO_2).